Robust Nonlinear Control of the HYDROÏD Humanoid Robotic Arm: A Comparative Study of Sliding Mode Strategies for High-Precision Trajectory Tracking

Youssef Mahmoud [1], Mohamed El Asswad [2], Ahmed Abdellatif [3*], Maya Sleiman [4], Khaled Khalil [5], and Samer Alfayad [6]

[1,3*] Arab Academy for Science, Technology and Maritime Transport (AASTMT), Mechanical Engineering Department, Sheraton Branch, Cairo, Egypt.
[2] Capgemini, Issy-les-Moulineaux, France.
[4,6] Université d'Évry Paris-Saclay, IBISC Laboratory, Évry, France.
[5] ECAM Rennes, Campus de Ker-Lann, Bruz, France.

Yusufali7319@gmail.com, mohamad.elasswad90@gmail.com, a_abdellatif@aast.edu, mayasleiman@ieee.org, khaled.khalil@ecam-rennes.fr, samer.alfayad@univ-evry.fr

Received: 26 April 2026 Accepted: 13 May 2026 Published: 17 June 2026

Abstract

This paper presents the modeling, control, and performance evaluation of a redundant 7-DOF anthropomorphic robotic arm of HYDROÏD humanoid hydraulic robot. A kinematic framework based on the Denavit–Hartenberg (D–H) convention is developed and integrated with a biomimetic design that embeds physiological motion constraints. To bridge theory and implementation, the system is modeled in a CAD-to-Simscape Multibody environment, capturing nonlinear actuator dynamics, torque saturation, and joint coupling. A comparative analysis is conducted between linear and robust nonlinear control strategies, including State Feedback, LQR, SMC, TSMC, and STSMC. The controllers are evaluated through tracking of complex trajectories—rectangle, infinity, and parallelogram—under disturbance and payload variation scenarios. Results show that sliding mode-based controllers significantly outperform linear approaches, reducing RMSE from over 20° (linear controllers) to below 10° (SMC variants). STSMC achieves the highest steady-state accuracy with MAE as low as 0.44°, while TSMC provides superior robustness with maximum deviation limited to approximately 0.83°. These findings confirm the effectiveness of advanced sliding mode strategies for high-DOF humanoid robotic systems operating under realistic conditions.

Key-words: Humanoid robotics, Sliding Mode Control, Robust nonlinear control, Trajectory tracking, Disturbance rejection

I. Introduction

Humanoid robotic manipulators have experienced rapid advancement in recent years, evolving toward increasingly sophisticated systems that closely resemble the structural and functional complexity of the human upper arm. These systems are typically modeled as high-degree-of-freedom (DOF) kinematic chains, enabling the execution of complex and dexterous tasks within environments originally designed for human interaction. However, achieving smooth and precise motion in such systems

* Corresponding Author

remains a fundamental challenge due to strong nonlinear dynamics, joint coupling, and sensitivity to parametric uncertainties and external disturbances [1-5].

Early developments in robotics primarily focused on fully autonomous industrial applications, where structured environments allowed for simplified control strategies. In contrast, recent research has shifted toward Human–Robot Collaboration (HRC), where robots operate alongside humans in dynamic and unstructured environments [6]. In these scenarios, the control problem extends beyond trajectory tracking to include safety, adaptability, and real-time responsiveness. Consequently, modern humanoid systems require advanced control frameworks capable of ensuring both high precision and robustness while maintaining stable interaction with uncertain and changing environments [7-8].

To contextualize this research, it is essential to examine recent developments in safety protocols and control architectures for collaborative robotics. A fundamental requirement in Human–Robot Collaboration (HRC) is the integration of safety mechanisms that protect operators during physical interaction. In this regard, Wang et al. [9] presented a neural-network-based real-time MPC framework for humanoid robot motion control. By combining DRNN with MPC and using a PDNN solver, the approach enables fast single-iteration optimization for multi-constrained kinematic control. The framework also addresses human–robot interaction safety through motion constraints, collision-aware behavior, and bounded joint and velocity limits.

Beyond safety, achieving mechanical transparency during physical interaction is equally critical. Compliance-based strategies, particularly those involving variable impedance or stiffness modulation, have been widely adopted to balance dynamic performance with intrinsic safety. These approaches allow robotic manipulators to adapt their mechanical behavior in real time, ensuring both precise motion and safe interaction under uncertain conditions [10]. Furthermore, the transition between free motion and constrained contact—commonly referred to as contact transition—introduces additional challenges due to abrupt changes in system dynamics. If not properly managed, this transition can lead to instability and high-impact forces. Recent studies have addressed this issue using force-based and hybrid control frameworks that regulate both motion and interaction forces, thereby maintaining stability and smooth behavior during contact events [11-12].

The precision requirements of Human–Robot Collaboration (HRC) demand control strategies capable of effectively handling the strong nonlinearities inherent in humanoid robotic systems. Sliding Mode Control (SMC) is widely employed in this context due to its robustness and strong disturbance rejection properties. However, its practical implementation is often limited by the chattering phenomenon, which introduces high-frequency oscillations that can degrade system performance and negatively affect actuator lifespan. To overcome this limitation, Jie et al. [13] used a sliding perturbation observer to estimate external environmental disturbances and modeling uncertainties. The proposed control scheme achieves high tracking precision, rapid convergence, and strong robustness against lumped uncertainties. These performance improvements are mainly attributed to the newly developed fractional-order terminal sliding surface and the disturbance estimation capability of the sliding perturbation observer.

The stability of the closed-loop system is rigorously analyzed using Lyapunov-based methods for both integer-order and fractional-order systems. Finally, experimental implementation on a real robotic manipulator validates the effectiveness and practical performance of the proposed control approach. Another approach has been used by Ambhore et al. [14]. Robot learning from demonstration is used as an approach that allows non-expert users to teach robots new tasks without complex reprogramming. It analyzes the formulation of the LfD problem and discusses different methods for acquiring and processing demonstration data. This research also reviews various learning approaches reported in the literature and highlights challenges related to demonstration quality, suboptimal examples, and evaluation metrics.

Humanoid robotic arms have attracted increasing research attention due to their ability to replicate human-like dexterity in complex and unstructured environments. However, their high degrees of freedom and strongly coupled nonlinear dynamics make precise trajectory tracking particularly challenging, especially in the presence of uncertainties, disturbances, and friction effects. To address these challenges, recent studies have focused on advanced nonlinear robust control strategies. For instance, Xu et al. [15] proposed a problem of fast adaptive trajectory tracking for robotic manipulators operating under parametric uncertainties and external disturbances. The authors developed kinematic and dynamic iterative algorithms based on screw theory for composite rigid-body systems and proposed a nonsingular terminal sliding-mode controller to improve tracking accuracy and convergence.

Adaptive compensation was used to reject lumped uncertainties, while a boundary layer was introduced to reduce the chattering effect commonly associated with sliding-mode control. The method was validated through Webots simulations on a 6-DoF GLUON-2L6-4L3 robotic manipulator. Similarly, Ahmed et al. [16] developed a robust model-free control for uncertain n-DOF robotic manipulators affected by external disturbances and backlash hysteresis. The proposed controller combined time delay control with adaptive terminal sliding-mode control to estimate unknown robot dynamics, improve robustness, and achieve finite-time convergence without requiring an accurate dynamic model. Adaptive tuning was introduced to handle bounded variations in the unknown dynamics, while Lyapunov-based analysis was used to prove system stability and determine the convergence rate. Simulation comparisons with an adaptive fractional-order terminal sliding-mode controller demonstrated the effectiveness and superiority of the proposed method under backlash hysteresis and disturbance conditions. More recently, Hosseinabadi et al. [17] introduced a fixed-time sliding mode observer-based controller capable of ensuring fast convergence and robustness without dependence on initial states, achieving a significant reduction in tracking error and improved disturbance rejection performance. These contributions clearly demonstrate that modern nonlinear robust control techniques—particularly higher-order and finite-time sliding mode approaches—play a crucial role in achieving high-precision, stable, and reliable trajectory tracking in humanoid robotic systems operating under realistic uncertainties.

The evolution of humanoid robotics has reached a critical bottleneck, where conventional metallic structures struggle to achieve the power-to-weight ratios required for dynamic and collaborative operation. Although hydraulic actuation offers superior power density and high force capabilities, its implementation in systems such as HYDROïD often leads to increased structural complexity due to the reliance on external piping and bulky manifolds. To address these limitations, recent research has explored Composite Hydraulic Integration, where fluid pathways are embedded directly within load-bearing components, enabling significant weight reduction and improved structural efficiency [18]. However, such integrated designs introduce additional challenges, including structural flexibility, nonlinear coupling effects, and increased sensitivity to disturbances. Consequently, controlling these systems requires advanced control architectures capable of maintaining high-precision trajectory tracking while ensuring robustness and real-time computational efficiency [19].

Despite the considerable progress achieved in nonlinear robust control and compliant interaction strategies, existing studies remain largely focused on individual control methodologies or simplified robotic platforms, often evaluated under limited or idealized conditions. In particular, there is a lack of comprehensive comparative analyses that assess the relative performance of multiple advanced control strategies on high-DOF humanoid robotic systems operating under realistic disturbances, varying payloads, and complex trajectory profiles. Recent works have demonstrated the effectiveness of individual approaches such as sliding mode control, adaptive control, and impedance-based frameworks in improving tracking accuracy and robustness [13-17]. However, these studies rarely provide a unified evaluation framework that captures performance trade-offs across different operational scenarios.

To address this gap, this paper presents a systematic and exhaustive performance analysis of several advanced control strategies applied to the HYDROïD humanoid robotic arm. The proposed study evaluates controller performance across multiple trajectory geometries and disturbance conditions, enabling a detailed comparison in terms of tracking accuracy, robustness, and computational efficiency. By quantifying these metrics within a consistent simulation framework, this work establishes a practical benchmark for selecting suitable control strategies for humanoid robotic systems engaged in real-world collaborative tasks.

The remainder of this paper is organized as follows. Section III presents the kinematic modeling and inverse kinematics formulation of the 7-DOF HYDROïD robotic arm. Section IV develops the dynamic model and details the design of both linear and nonlinear control strategies, including State Feedback, LQR, SMC, TSMC, and STSMC. Section V introduces the Simscape Multibody simulation framework and the trajectory generation approach. Section VI presents a Simulation Framework, while Section VII discusses the comparative performance results across multiple trajectory profiles. Finally, Section VIII concludes the paper with final remarks and future research directions.

II. Problem statement

The development of high-performance humanoid robotic arms presents a fundamental trade-off between achieving high actuation force and maintaining a human-like weight profile. In hydraulic humanoid systems such as HYDROïD, hydraulic integrated parts (HIP) alone can account for nearly 50% of the total robot mass, with significant contributions from arm structures where internal manifolds and fluid channels are embedded within load-bearing components. Conventional metallic implementations, while structurally robust, lead to excessive weight, with the current prototype reaching approximately 125 kg compared to a target weight of 75 kg, necessitating a drastic weight reduction of nearly 40%.

To address this limitation, recent developments have introduced Composite Hydraulic Integration [20], where external piping is eliminated and replaced by internal fluid pathways embedded within structural components. This biomimetic approach, analogous to human vascular systems, enables improved flexibility, reduced leakage, and enhanced actuator bandwidth by removing pipe-induced stiffness. The proposed design combines additive manufacturing of thermoplastic polymers (e.g., PA-GF) with random fiber composite reinforcement (e.g., CF/Epoxy), forming a multi-layer structure capable of sustaining high internal pressures while significantly reducing mass.

However, this transition introduces new challenges. The integrated internal channels must withstand pressures exceeding 150 bar while maintaining structural integrity under coupled mechanical and hydraulic loading conditions. Additionally, the use of lightweight composite materials alters the dynamic characteristics of the system, introducing structural flexibility, modified resonance frequencies, and increased sensitivity to disturbances. These factors result in uncertain nonlinear dynamics, complex coupling between joints, and potential degradation in tracking performance. From a control perspective, these challenges define a nonlinear trajectory tracking problem under significant uncertainties, including parametric variations, unmodeled dynamics, and disturbance forces arising from hydraulic actuation and friction. Furthermore, due to the complexity of the full 7-DOF humanoid arm, this study focuses on a representative 4-DOF subsystem, capturing the dominant motion dynamics while enabling efficient evaluation of advanced control strategies. The objective is to design robust control laws capable of compensating for the nonlinearities and structural uncertainties introduced by the composite hydraulic architecture, while ensuring high tracking precision and real-time computational efficiency.

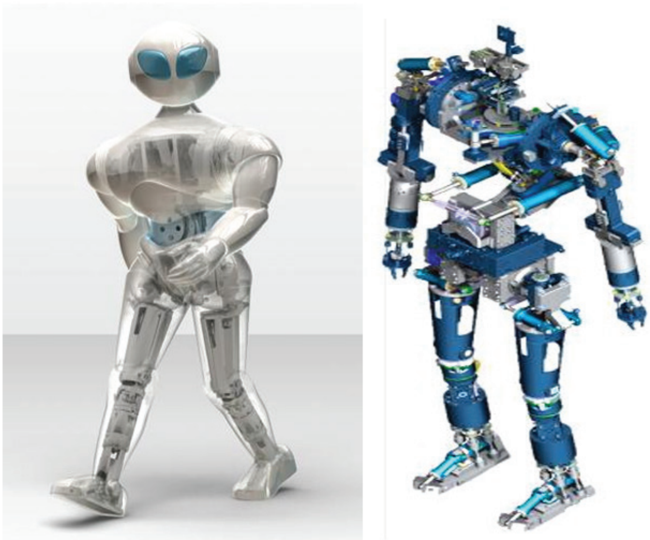

Figure 1: HYDROÏD robot full CAD model.

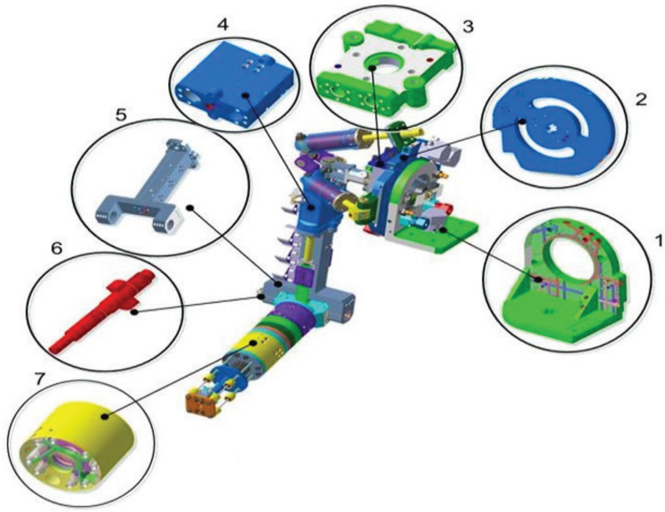

Figure 2: Exploded view of the HYDROÏD robotic arm illustrating the hydraulic integrated components: (1) Shoulder upper part, (2) Shoulder middle part, (3) Shoulder lower part, (4) Elbow upper part, (5) Elbow lower part, (6) Elbow axis of rotation, and (7) Wrist part.

Current manufacturing limitations make it difficult to shape high-strength composites into the intricate internal geometries required for fluid transport. As illustrated in the detailed breakdown of the arm components in Fig. 2, the integration of these "internal veins" within the structural chassis is a complex engineering task. This study addresses these challenges by focusing exclusively on the control of a 4-DOF subset of the HYDROïD system. By implementing advanced nonlinear control laws, we aim to compensate for the structural complexities and potential elasticities of the integrated composite design while maintaining low computational overhead.

III. Kinematic modeling

In this section, the forward and inverse kinematic formulations of the complete 7-DOF kinematic chain are developed. The forward kinematics establishes the nonlinear mapping from joint space to end-effector position and orientation, while the inverse kinematics determines the required joint variables for a desired Cartesian trajectory. Given the redundancy of the system, special attention is given to the existence of multiple solutions and the selection of feasible configurations that satisfy mechanical constraints and task requirements.

A. *Forward Kinematics (FK)*

Forward kinematics (FK) is used to determine the end-effector's position and orientation based on individual joint angles. By assigning coordinate frames to the links as shown in Fig. 3, we utilize the (D-H) convention to represent these spatial relationships. The specific geometric constants, including link lengths and offset angles for the 7-DOF assembly, are detailed in the parameter set shown in Fig. 4. Each joint's transformation is defined by a homogeneous matrix T_i, and the total transformation from the base to the end-effector is represented by the chain:

$$T_{\text{base}}^{\text{EE}} = T_1^0 \cdot T_2^1 \cdot T_3^2 \cdot T_4^3 \cdot T_5^4 \cdot T_6^5 \cdot T_7^6 \qquad (1)$$

The resulting position vectors and rotation matrices are extracted from this final transformation matrix $T_{\text{base}}^{\text{EE}}$ to define the robot's pose in 3D space.

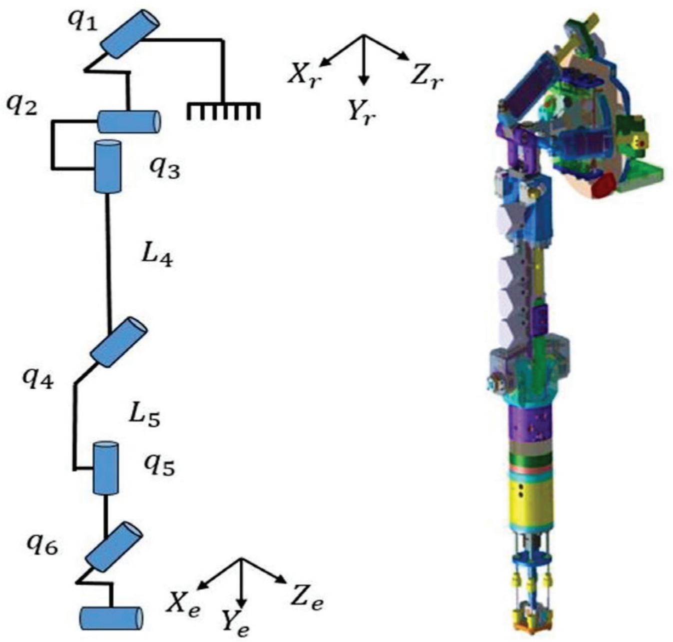

Figure 3: Kinematic model and coordinate frames for the 7-DOF HYDROïD robot arm.

Denavit Hartenberg Notation				
i	$\mathbf{q_i}$	$\boldsymbol{\alpha_i}$	$\mathbf{a_i}$	$\mathbf{b_i}$
1	q_1	0	0	0
2	$q_2 - \frac{\pi}{2}$	$\frac{\pi}{2}$	0	0
3	$q_3 - \frac{\pi}{2}$	$\frac{\pi}{2}$	0	0
4	$q_4 - \pi$	$\frac{\pi}{2}$	L_4	0
5	q_5	0	L_5	0
6	$q_6 + \frac{\pi}{2}$	$\frac{\pi}{2}$	0	0
7	$q_7 + \frac{\pi}{2}$	$\frac{\pi}{2}$	0	0

Figure 4: (D-H) parameters for the HYDROïD 7-DOF arm.

B. *Inverse Kinematics (IK)*

To follow complex trajectories like the infinity or parallelogram paths, the system must solve the Inverse Kinematics problem—calculating the specific configurations required for the 7-DOF arm to reach a target position P. Due to the redundant nature and high nonlinearity of the HYDROïD arm, we employ the Jacobian inverse method. The relationship between Cartesian velocities $\dot{x}$ and joint velocities $\dot{q}$ is expressed as:

$$\dot{x} = J(q)\dot{q} \tag{2}$$

To determine the required joint rates:

$$\dot{q} = J^{+}(q)\dot{x} \tag{3}$$

To determine the required joint velocities, the Moore–Penrose pseudoinverse of the Jacobian matrix is employed. This approach allows the system to handle kinematic redundancy while ensuring a feasible solution for joint space motion. This iterative calculation ensures the end-effector tracks the reference trajectory accurately while maintaining the structural constraints of the composite assembly.

IV. System architectural and constraints

A. *Joint configuration & anatomical mapping*

The structural architecture of HYDROïD is centered on a high-fidelity anthropomorphic design, utilizing a redundant 7-DOF kinematic chain to mirror the dexterity of the human upper arm. Unlike standard lower-order systems, this configuration allows the robotic arm to perform complex maneuvers while maintaining human-like reaching profiles. The system is functionally categorized into three primary anatomical regions: the shoulder complex, the elbow joint, and the wrist mechanism.

The shoulder complex is driven by the first four degrees of freedom. Joint 1 is the Shoulder Girdle (SG), which provides lateral positioning. Joint 2 and Joint 4—Shoulder Flexion/Extension (SFE) and Shoulder Abduction/Adduction (SAA)—serve as the primary drivers for vertical and lateral arm elevation. To simulate the axial rotation of the humerus, Joint 3 (Shoulder Vertical) is incorporated. The elbow region consists of Joint 5 (Elbow Vertical) for rotational alignment and Joint 6 Elbow Flexion (EF) for reach-and-retract actions. Finally, Joint 7 Wrist Abduction/Adduction (WAA) provides the necessary precision for end-effector orientation.

B. Biomechanical constraints & operational envelopes

To ensure safe operation during interaction tasks, the robotic arm is engineered to operate strictly within biological motion limits. These biomechanical constraints are integrated as fundamental parameters within the kinematic basis A_i, ensuring that all trajectory calculations naturally adhere to an ergonomic envelope. As detailed in Table 1, the motion ranges are strictly defined to prevent mechanical interference. For example, the Shoulder Girdle (SG) is restricted to ±30°, and the Shoulder Flexion (SFE) varies between -10° and +125°, replicating the lifting action of the human arm. The wrist movements are constrained to ±45°, offering sufficient flexibility for task-space manipulation without compromising joint stability.

Table 1: Biomimetic parameters and actuator constraints.

Joint ID	Anthropomorphic Equivalent	Range of Motion (deg)	Max Speed (deg/s)	Max Torque (N·m)
Joint 1	Shoulder Girdle (SG)	±30	120	180
Joint 2	Shoulder Flexion (SFE)	-10 to +125	180	260
Joint 3	Shoulder Vertical (SV)	±50	160	300
Joint 4	Shoulder Abduction (SAA)	-30 to +120	180	280
Joint 5	Elbow Vertical (EV)	±90	220	70
Joint 6	Elbow Flexion (EF)	-5 to +90	200	65
Joint 7	Wrist Abduction (WAA)	-45 to +45	220	15

C. Dynamic saturation and power constraints

To achieve high fidelity in the Simscape environment, the system accounts for nonlinear actuator limits, specifically torque and velocity saturation. The shoulder joints are equipped with high-torque actuators (up to 300 N·m) to manage the inertial effects of the entire arm. Conversely, the distal joints are optimized for higher speeds to facilitate rapid end-effector adjustments. By embedding these physical limits, we ensure that the performance evaluation of the STSMC, SMC, and LQR controllers accurately reflects real-world hardware behavior under limited power resources.

V. Dynamic modeling and control design

A. Dynamic formulation

The mechanical behavior of a humanoid arm is characterized by a set of second-order nonlinear differential equations. To provide a rigorous framework for the comparative control analysis, the system is modeled using the Euler-Lagrange principle, which maps the relationship between joint torques and the resulting motion. The governing dynamic equation is expressed as:

$$M(q)q'' + C(q,q')q' + G(q) + F(q') = \tau + \tau_d \quad (4)$$

Where q, q', and $q'' \in \mathbb{R}^4$ represent the vectors of angular position, velocity, and acceleration for the SG, SFE, EF, and WAA joints, respectively. In this formulation, $M(q) \in \mathbb{R}^{4x4}$ is the symmetric positive-definite inertia matrix, $C(q,q') \in \mathbb{R}^{4x4}$ denotes the Coriolis and centrifugal force matrix, and $G(q) \in \mathbb{R}^4$ is the gravitational torque vector. The term $F(q')$ represents the friction vector, incorporating both viscous and Coulomb models, while τ and τ_d denote the control input and external disturbance torques, respectively.

B. Computational dynamics & Simscape integration

To ensure high-fidelity performance during the simulation phase, the physical parameters of the 4-DOF manipulator were derived through an automated CAD-to-Multibody synchronization process. By utilizing the volumetric mass properties and spatial constraints defined in the original engineering assembly, the model was integrated into the Simscape Multibody environment. This approach allows for the automatic and precise computation of the nonlinear dynamics, including the configuration-dependent inertia matrix $M(q)$, the gravity vector $G(q)$, and the complex Coriolis and centrifugal effects $C(q,q')$.

Furthermore, the simulation environment incorporates a detailed friction model $F(q')$ at each joint and accounts for the cumulative resistance and unmodeled dynamics represented by τ_d. By including these resistive torques and the effects of additional payloads in the multibody plant, the "Digital Twin" provides a realistic and challenging platform. This ensures that the subsequent comparison of the controllers is based on a model that accounts for the actual mechanical offsets, energy losses, and external perturbations inherent in the physical 4-DOF system.

C. *Linear control strategies*

To facilitate the design of linear control strategies, the nonlinear dynamic model in (4) is linearized about a nominal operating point to obtain the state-space representation:

$$x' = Ax + Bu \tag{5}$$

Where $x \in \mathbb{R}^8$ is the state vector representing the joint positions and velocities, and u is the control torque vector.

1. State feedback control

The first linear strategy employs a state feedback architecture where the control action is derived from the full state vector of the 4-DOF manipulator. The core objective of this controller is to modify the natural dynamics of the system by applying a gain matrix to the measured states. The primary tuning parameters for this controller are the desired closed-loop poles. By strategically placing these poles further into the negative real region of the complex plane, the controller can be tuned to provide a faster transient response and significantly reduce the rise time. However, a trade-off exists: more aggressive pole placement requires higher control effort, which can lead to actuator saturation or the amplification of high-frequency sensor noise. The gain matrix is computed such that the resulting closed-loop system matrix remains strictly stable.

The corresponding control law and system stability conditions are defined as:

$$u = -Kx \tag{6}$$

$$\det\big(\lambda I - (A - BK)\big) = 0 \tag{7}$$

2. Linear Quadratic Regulator (LQR)

To achieve a more balanced performance compared to standard pole placement, an LQR controller is implemented. This method treats control as an optimization problem rather than a manual assignment of poles. The performance of the LQR controller is primarily governed by two tuning parameters: the State Weighting Matrix Q and the Control Weighting Matrix R.

By increasing the values in the Q matrix, the controller is forced to prioritize tracking precision, which leads to faster error convergence and higher accuracy. Conversely, increasing the values in the R matrix penalizes control effort, which results in smoother torque commands that protect the 4-DOF manipulator's motors from mechanical stress and overheating. The controller automatically calculates the optimal gain matrix K that minimizes the total cost based on the specific ratio between these two matrices.

The cost function used for this optimization and the resulting control law are expressed as follows:

$$J = \int_0^{\infty} (x^T Q x + u^T R u)dt \tag{8}$$

$$u = -Kx \tag{9}$$

D. *Robust nonlinear control strategies*

While linear controllers are effective near specific operating points, a high DOF arm exhibits significant nonlinearities and is subject to external disturbances. To achieve high-precision tracking across the entire workspace, robust nonlinear control strategies are employed. These methods utilize the full dynamic model of the system to ensure stability and rejection of perturbations such as friction and varying payloads.

1. Sliding Mode Control (SMC)

The first nonlinear strategy is a robust Sliding Mode Controller, which is designed to handle the nonlinearities identified in our model. The controller operates by forcing the system state to reach and stay on a predefined manifold known as the Sliding Surface s. The performance and behavior of this controller are governed by two primary parameters:

- **Sliding Surface Coefficient λ :** This parameter defines the slope of the surface. A higher value of λ results in a faster exponential convergence of the tracking error toward zero once the system is on the surface.

- **Switching Gain η :** This gain determines the "strength" of the controller in rejecting disturbances. It is tuned to ensure that the system stays bound to the sliding manifold despite model uncertainties.

To eliminate the chattering phenomenon—the high-frequency torque oscillations that can damage the robot's actuators—the traditional signum function is replaced with a continuous hyperbolic tangent function $\tanh$. This creates a smooth transition across the sliding surface, ensuring the control torque is physically feasible for the motors while maintaining robust tracking.

The sliding surface, the continuous control law, and the stability conditions are defined as:

$$s = e' + \lambda e \tag{10}$$

$$u = M(q)(q''_d + \lambda e') + C(q, q')q' + G(q) + F(q') + \eta \tanh(s) \tag{11}$$

To verify the stability and controllability of the system, a Lyapunov candidate function is chosen as shown in (12). By taking the time derivative of this function, we derive the reaching condition in (10). As shown in equation (13), since the derivative of the Lyapunov function is negative-definite, we determine that the system is globally stable and controllable, as the tracking error is mathematically guaranteed to reach the sliding surface.

$$V = \left(\frac{1}{2}\right) s^2 \tag{12}$$

$$\dot{V} = s \cdot s' \le -\eta |s| \tag{13}$$

2. Terminal Sliding Mode Control (TSMC)

To achieve faster convergence and enhanced tracking precision, a Terminal Sliding Mode Controller is implemented. This version utilizes the same linear sliding surface as the SMC but incorporates a dual-gain reaching law within the control function. This structure allows for a more aggressive response to position and velocity errors, effectively forcing the system state toward the origin more rapidly.

The performance of this controller is governed by the following parameters:

- **Position Error Gain k_1:** The primary gain acting on the position error to drive the system toward the sliding manifold.

- **Velocity Error Gain k_2:** A stabilizing gain acting on the velocity error to provide damping and prevent overshoot.

The mathematical model for this controller is expressed as follows:

$$s = e' + \lambda e \tag{14}$$

$$u = M(q)(q''_d + \lambda e') + C(q, q')q' + G(q) + F(q') + k_1 e + k_2 e' + \eta \tanh(s) \tag{15}$$

Stability is confirmed via the Lyapunov method. As shown in equation (17), the negative-definite derivative of the energy function ensures that the tracking error is mathematically guaranteed to reach the sliding surface and remain stable throughout the operation.

$$V = \left(\frac{1}{2}\right) s^2 \tag{16}$$

$$\dot{V} = s \cdot s' \le -\eta |s| \tag{17}$$

3. Super-Twisting Sliding Mode Control (STSMC)

The final nonlinear strategy implemented is the Super-Twisting Sliding Mode Controller (STSMC). As a second-order sliding mode technique, the STSMC is specifically designed to eliminate the chattering phenomenon without sacrificing robustness. Unlike traditional first-order sliding mode controllers, the STSMC confines the switching action to the higher-order derivatives of the sliding manifold. By replacing the discontinuous signum function with a continuous $\tanh$ function, the controller provides a smooth, high-precision torque output that is physically ideal for HYDROïD actuators.

The performance of this controller is governed by two main gains:

- **Sliding Gain k_1:** This gain drives the system state toward the sliding surface and ensures convergence.
- **Integral Gain k_2:** This gain acts on the integral component of the reaching law, providing the necessary effort to cancel out model uncertainties and disturbances.

The sliding surface and the combined super-twisting control law are defined as follows:

$$s = e' + \lambda e \tag{18}$$

$$u = M(q)(q_d'' + \lambda e') + C(q, q')q' + G(q) + F(q') + k_1|s|^{\frac{1}{2}}\tanh(s) + \int (k_2 \tanh(s))dt \tag{19}$$

Stability for the STSMC is verified using the Lyapunov method. As shown in equation (21), the negative-definite nature of the derivative ensures that the system is globally stable and the tracking error is mathematically guaranteed to reach the sliding surface.

$$V = \left(\frac{1}{2}\right)s^2 \tag{20}$$

$$\dot{V} = s \cdot s' \leq -\eta|s| \tag{21}$$

VI. Simulation Framework

A. *Dynamic disturbances & payload scenarios*

To ensure the controllers are capable of operating in real-world industrial environments, the simulation incorporates two distinct types of system perturbations. First, external disturbances are introduced into the joint dynamics to represent unpredictable environmental factors, such as friction variations and unmodeled forces.

Second, the system is subjected to a payload-varying scenario that mimics a "pick-and-place" operation. In this phase, the humanoid arm carries a heavy payload that is dropped midway through the simulation. This action causes an instantaneous change in the robot's mass properties and inertia. These challenges are designed to test the robustness of the SMC, TSMC, and STSMC strategies, specifically observing how effectively the control laws can reject these disturbances while maintaining trajectory accuracy.

B. *Trajectory profiles & motion parameterization*

To evaluate the tracking precision and adaptability of the SMC, TSMC, and STSMC controllers, HYDROïD was tasked with following three distinct geometric paths: A Rectangle, an Infinity symbol, and a Parallelogram.

While each path represents a different spatial challenge—ranging from sharp 90° turns in the rectangle to continuous curvature in the infinity symbol and slanted linear movements in the parallelogram—they all share a unified motion profile.

To ensure the trajectories are physically feasible while maintaining high real-time performance, every segment of these paths is generated using a 4th-degree (quartic) polynomial function.

This specific order was selected to satisfy the boundary conditions for position and velocity at the start and end of each segment. By utilizing a 4th-degree profile rather than higher-order functions, we successfully minimize the computational complexity of the trajectory generator. This reduction in mathematical overhead ensures that the controller can prioritize the high-frequency execution of the sliding mode laws. Each coordinate (X, Y, Z) is thus governed by:

$$p(t) = a_0 + a_1 t + a_2 t^2 + a_3 t^3 + a_4 t^4 \quad (22)$$

The successful output of this function is a continuous set of Cartesian reference commands. These are then processed through the inverse kinematics model to generate the joint-space trajectories that the end-effector must follow. By using this quartic parameterization, we can accurately measure how well each controller maintains the geometric integrity of these shapes when subjected to the external disturbances and payload drops previously described.

C. System architecture & simulation framework

The robotic arm is implemented within a MATLAB/Simscape environment. Although the HYDROÏD arm is physically designed as a 7-DOF redundant manipulator, this study focuses on the implementation and performance analysis of a 4-DOF subset. This subset includes the Shoulder Yaw (SY), Shoulder Pitch (SP), Elbow Pitch (EP), and Wrist Roll (WR), which constitute the primary high-torque joints responsible for the arm's spatial positioning.

The initial stage of the control pipeline involves transforming task-space objectives into joint-space commands.

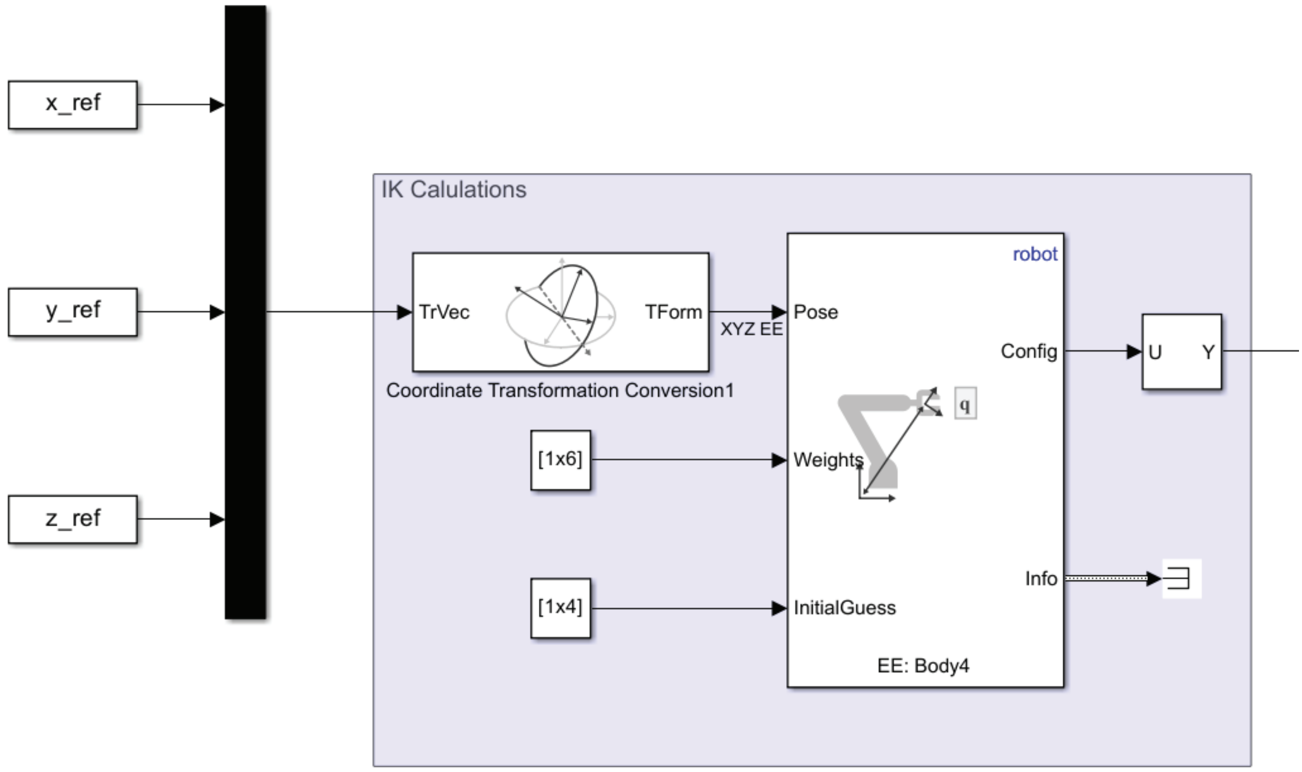

Figure 5: Inverse Kinematics (IK) subsystem architecture.

As illustrated in Fig. 5, the Cartesian reference inputs x_{ref}, y_{ref}, and z_{ref} are processed through a Coordinate Transformation Conversion block. The resulting pose is fed into the IK Calculation block, which utilizes a rigid body tree model of the robot. This block calculates the necessary joint configurations q_1 through q_4 required to reach the desired end-effector position.

1. Error dynamics & signal feedback

Once the reference configurations are generated, the system calculates the real-time state error to drive the controllers. In Fig. 6, the desired joint positions and velocities are compared against the actual feedback signals from the plant. The system computes the position error and velocity error for each of the four joints. These error signals are then multiplexed and sent to the respective control blocks, ensuring that each joint is managed independently.

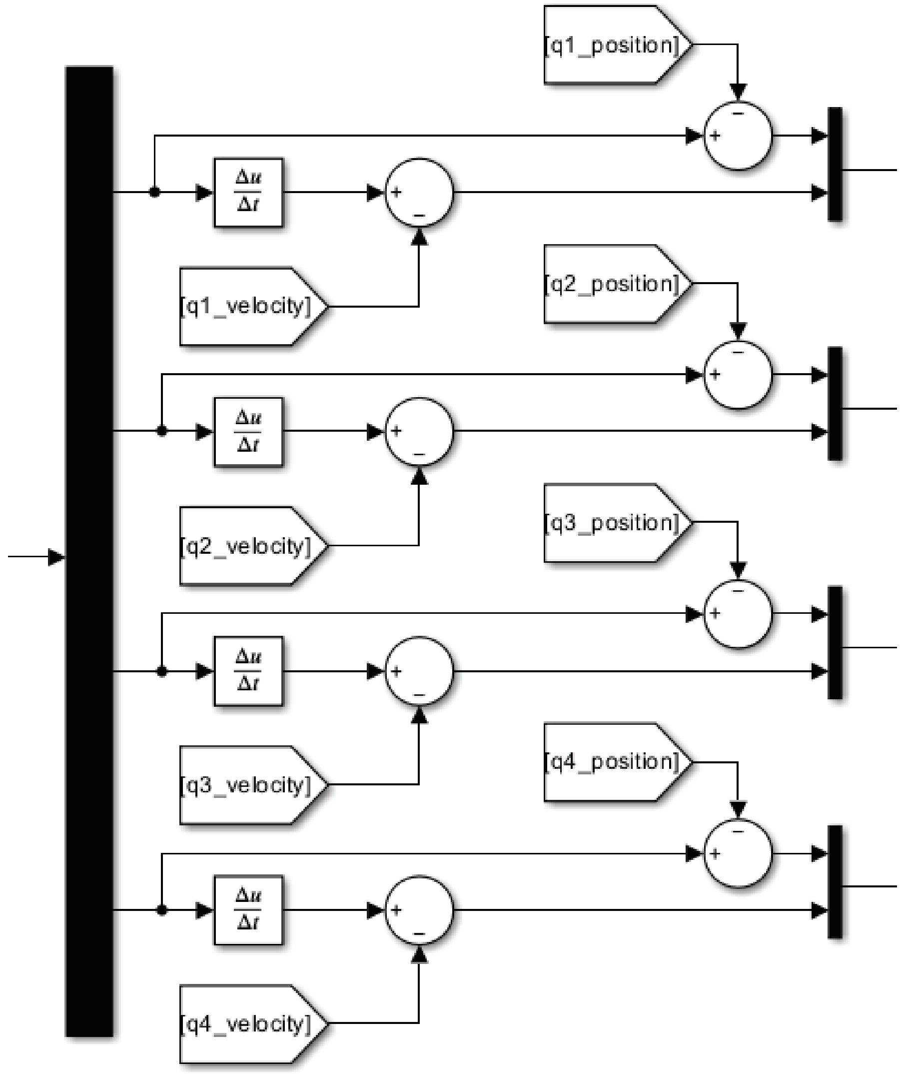

Figure 6: Feedback loop and error calculation manifold.

2. Nonlinear control & disturbance injection

The core of the simulation lies in the execution of the control laws and the introduction of environmental stressors.

As shown in Fig. 7, the pipeline utilizes four dedicated controller blocks (one for each specific joint). During testing, these blocks are swapped to compare the performance of State Feedback, LQR, SMC, TSMC, and STSMC. Before the calculated torque reaches the robot, it passes through the Environment Disturbance blocks. These blocks inject the unmodeled forces and payload variations (such as the [5 kg] pick-and-drop scenario) to test the robustness of the control strategies.

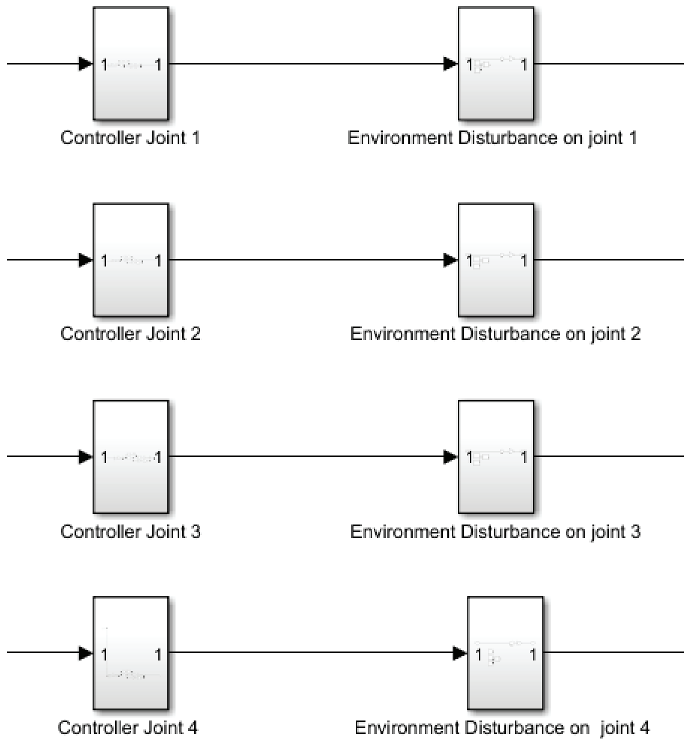

Figure 7: Control modules and environment disturbance blocks.

3. Physical plant and data acquisition

The final stage is the Simscape Multibody representation of the physical robot and the extraction of simulation results. The physical dynamics are handled by the Robot Plant block (Fig. 8), which accounts for mass, inertia, and gravitational effects. While the system may possess additional degrees of freedom, the control and data acquisition focus exclusively on the four joints shown. The resulting actual positions $q_{position}$ and velocities $q_{velocity}$ are then exported to the MATLAB workspace for analysis.

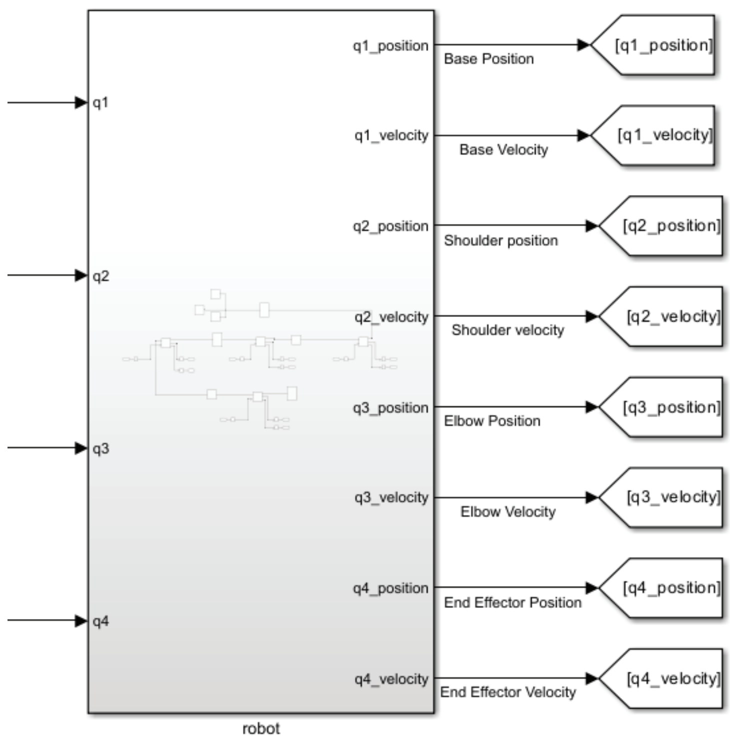

Figure 8: Simscape Multibody plant and data extraction points.

VII. Results and Discussion

In this section, the performance of the five control strategies—Decoupled State Feedback, LQR, SMC, TSMC, and STSMC—is evaluated. The analysis is divided into three subsections, one for each trajectory, focusing on visual tracking response and global numerical metrics.

A. *Parallelogram trajectory analysis*

The parallelogram trajectory assesses the coordination of joints during slanted linear movements, requiring simultaneous and precise control of all four degrees of freedom. The tracking performance for each joint is illustrated in Fig. 9 through Fig. 12.

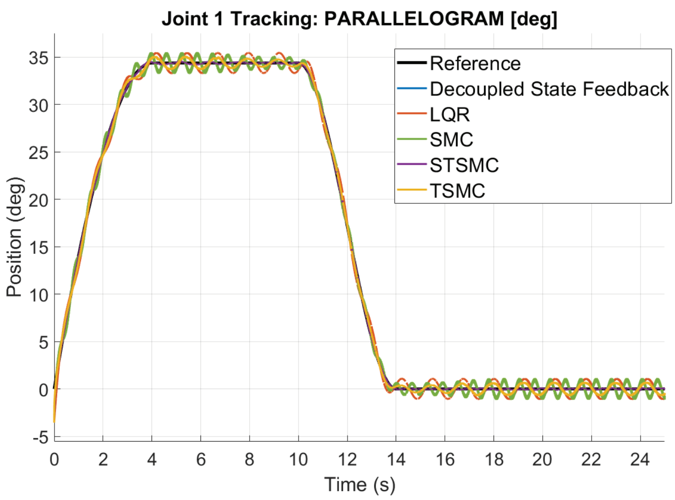

Figure 9: Joint 1 position tracking for the Parallelogram trajectory.

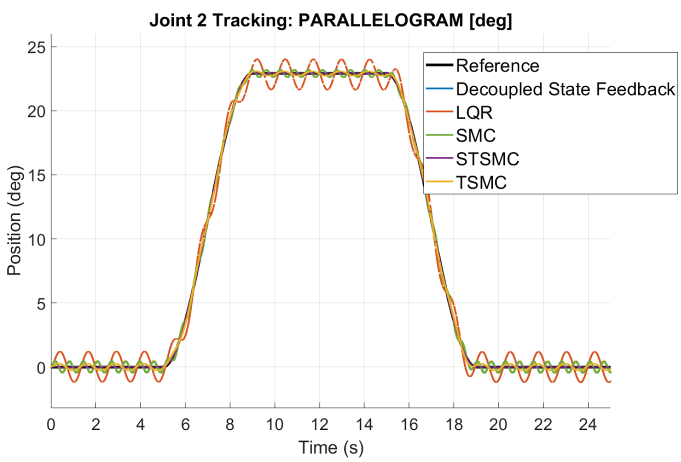

Figure 10: Joint 2 position tracking for the Parallelogram trajectory.

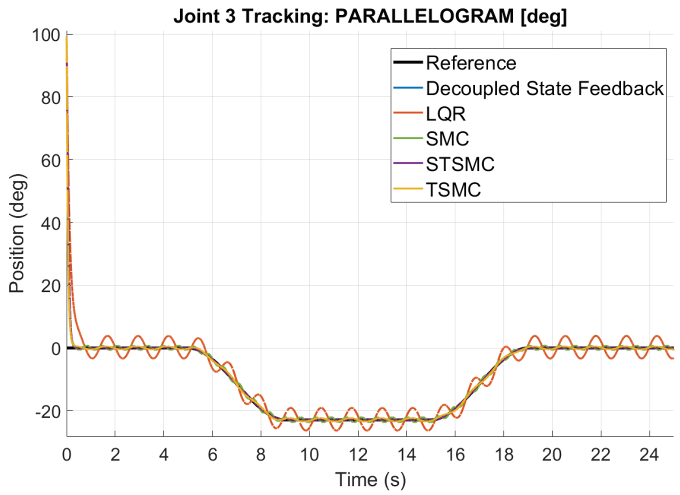

Figure 11: Joint 3 position tracking for the Parallelogram trajectory.

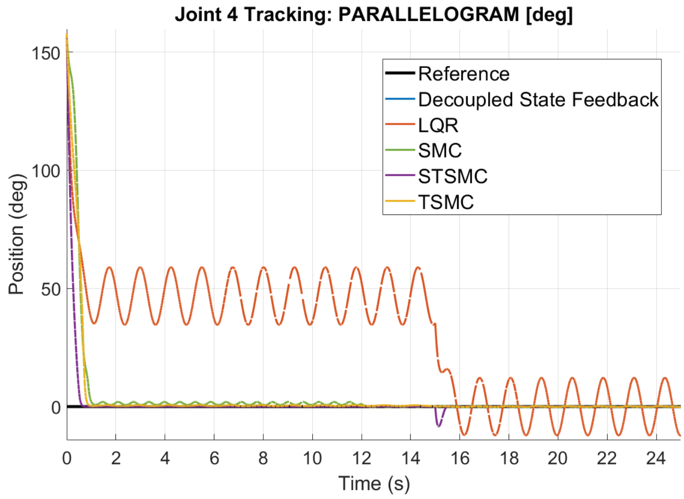

Figure 12: Joint 4 position tracking for the Parallelogram trajectory.

The position tracking results across all four joints (Figs. 9–12) reveal a clear distinction between linear and nonlinear control capabilities. The Decoupled State Feedback and LQR controllers exhibit significant steady-state oscillations and struggle to maintain the path during the constant-velocity segments of the parallelogram. In contrast, the sliding mode variants (SMC, TSMC, and STSMC) show much tighter convergence to the reference signal, with STSMC providing the smoothest transition at the trajectory's vertices.

To provide a precise comparison of these behaviors, the aggregated performance metrics for this trajectory are summarized in Table 2. These metrics are defined as follows:

- **Root Mean Square Error (RMSE):** This parameter represents the total energy of the error signal across all joints, providing an indication of the overall stability of the control system.

- **Mean Absolute Error (MAE):** This metric calculates the average tracking deviation throughout the simulation, serving as the primary indicator for general steady-state accuracy.

- **Maximum Deviation (D_{max}):** This value captures the largest single error recorded during the steady-state or disturbance phase, specifically measuring the robustness of the controller against external perturbations.

Table 2: Global performance metrics for parallelogram trajectory.

Controller	RMSE (deg)	MAE (deg)	D_{max} (deg)
Decoupled State Feedback	20.2483	8.7740	59.0398
LQR	20.2615	8.7798	59.0396
SMC	9.4399	1.2802	2.0521
STSMC	5.7730	0.4449	8.4813
TSMC	8.4286	0.9816	0.8285

1. Discussion & Recommendations:

- **Steady-State Precision:** For the parallelogram path, the STSMC is the most recommended controller for tasks requiring high precision. It achieved the lowest average tracking error with an MAE of only 0.4449°. This performance proves that the super-twisting algorithm is highly effective at driving the joint error variables e_1 through e_4 toward zero while maintaining a smooth control signal.

- **Peak Robustness:** When evaluating the system's ability to manage the discontinuous velocity changes at the trajectory vertices, TSMC is the superior choice. It maintained a D_{max} of only 0.8285°, which is significantly lower than the 8.4813° recorded for STSMC. This suggests that the terminal sliding manifold provides a more decisive restoration of the state variables to the reference path whenever external perturbations or cornering forces cause a deviation from the sliding surface.

- **Control Limitations:** The linear strategies—Decoupled State Feedback and LQR—showed an RMSE of approximately 20.2°. These high values confirm that linear control cannot adequately compensate for the nonlinear gravitational effects and joint coupling experienced during this trajectory.

B. *Rectangle trajectory analysis*

The rectangle trajectory evaluates the manipulator's ability to maintain linear precision while navigating abrupt orientation changes at sharp 90° corners. The tracking performance for joints q_1 through q_4 is illustrated in Figs. 13 through 16.

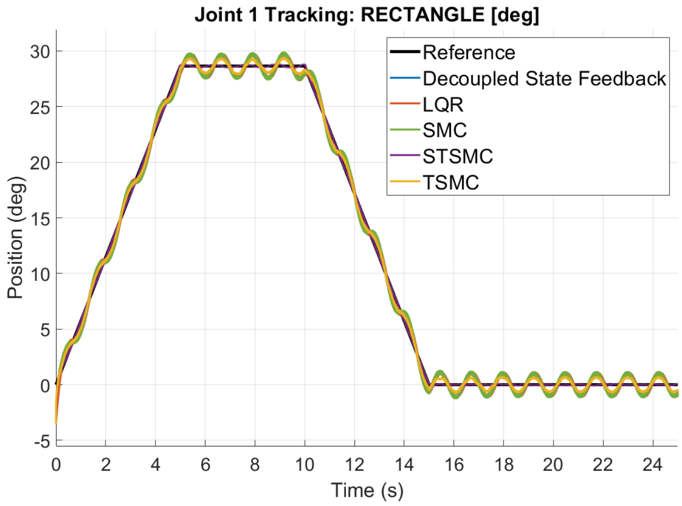

Figure 13: Joint 1 position tracking for the Rectangle trajectory.

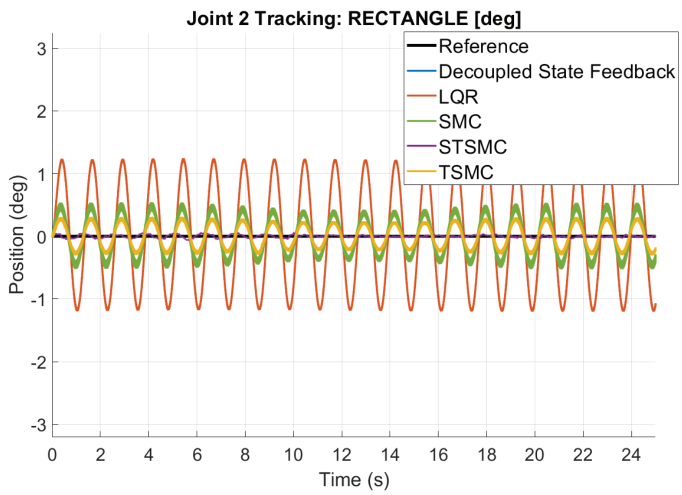

Figure 14: Joint 2 position tracking for the Rectangle trajectory.

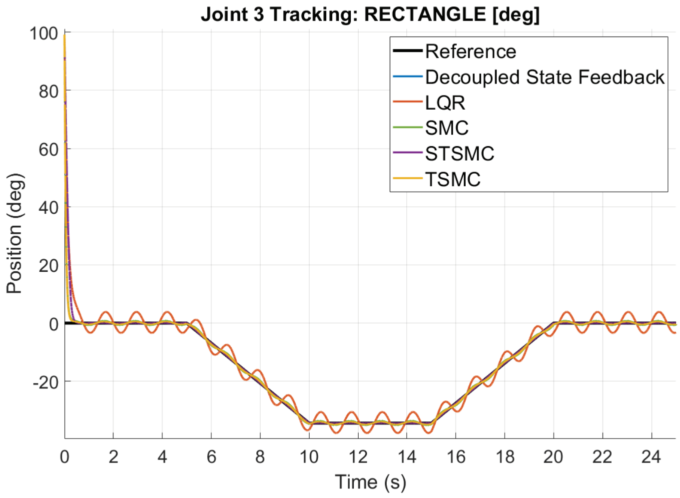

Figure 15: Joint 3 position tracking for the Rectangle trajectory.

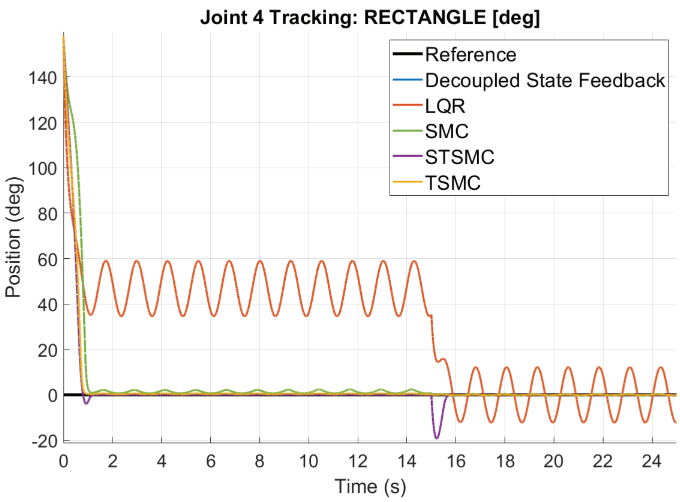

Figure 16: Joint 4 position tracking for the Rectangle trajectory.

The tracking results in Figs. 13–16 highlight the impact of the trajectory's corners on control stability. While the sliding mode controllers successfully complete the path, the STSMC and SMC exhibit visible deviations at each vertex where the velocity vector changes instantaneously. The linear controllers (LQR and State Feedback) show severe overshoot at these points, failing to damp the oscillations quickly enough to maintain the rectangular geometry.

To provide a precise comparison of these behaviors, the aggregated performance metrics for this trajectory are summarized in Table 3. These metrics are defined as follows:

- **Root Mean Square Error (RMSE):** Represents the total error energy, indicating overall system stability.
- **Mean Absolute Error (MAE)**: Calculates the average tracking deviation, serving as the primary indicator for general accuracy.
- **Maximum Deviation (D_{max}):** Captures the largest single error recorded after the initial transient, measuring robustness against sharp trajectory transitions and disturbances.

Table 3: Global performance metrics for rectangle trajectory.

Controller	RMSE (deg)	MAE (deg)	D_{max} (deg)
Decoupled State Feedback	20.4156	9.4048	59.0397
LQR	20.4035	9.3950	59.0396
SMC	10.6308	1.5739	2.8456
STSMC	8.7480	0.8583	19.2924
TSMC	8.4396	0.9977	0.8297

1. Discussion & Recommendations:

- **Steady-State Accuracy:** Despite the sharp corners, STSMC provides high average precision with an MAE of 0.8583°. However, its performance is noticeably affected compared to smoother paths, as the super-twisting law requires a finite time to adapt to the abrupt acceleration changes at the vertices.
- **Superior Robustness:** For this specific trajectory, TSMC is the most recommended controller. It maintained an exceptionally low D_{max} of 0.8297°, whereas the STSMC experienced a peak deviation of 19.2924°. This confirms that the terminal sliding manifold is highly effective at constraining error growth during non-smooth reference transitions.
- **System Stability:** The RMSE values demonstrate that TSMC 8.4396° and STSMC 8.7480° provide comparable overall stability, both significantly outperforming the linear methods, which maintained errors above 20.4°.

C. *Infinity trajectory analysis*

The infinity trajectory assesses the manipulator's coordination during complex, synchronized motion across all degrees of freedom. The tracking performance for joints q_1 through q_4 is illustrated in Figs. 17 through 20.

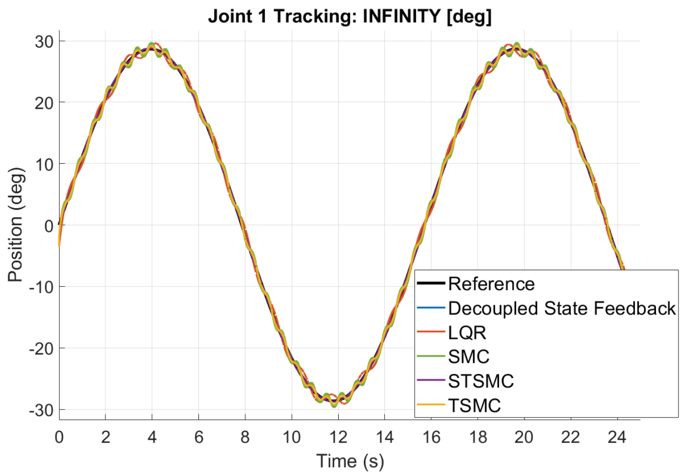

Figure 17: Joint 1 position tracking for the Infinity trajectory.

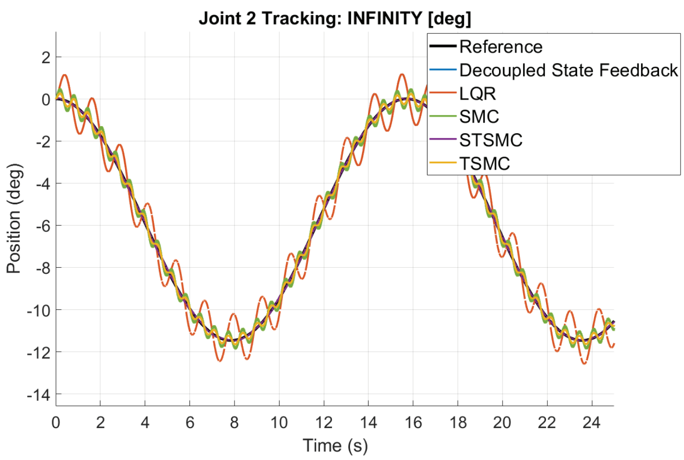

Figure 18: Joint 2 position tracking for the Infinity trajectory.

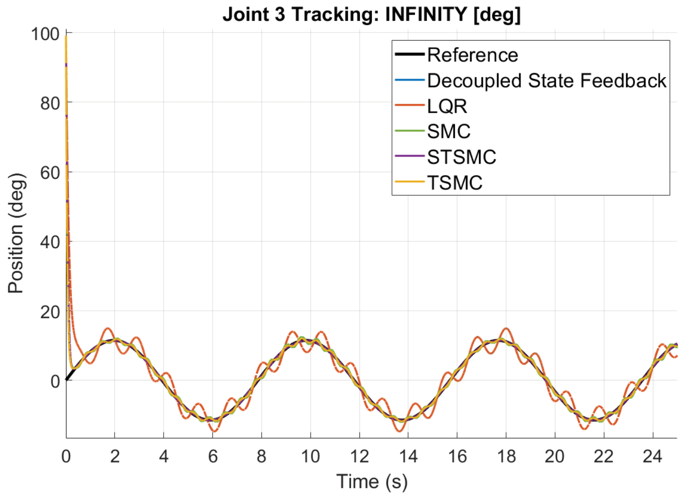

Figure 19: Joint 3 position tracking for the Infinity trajectory.

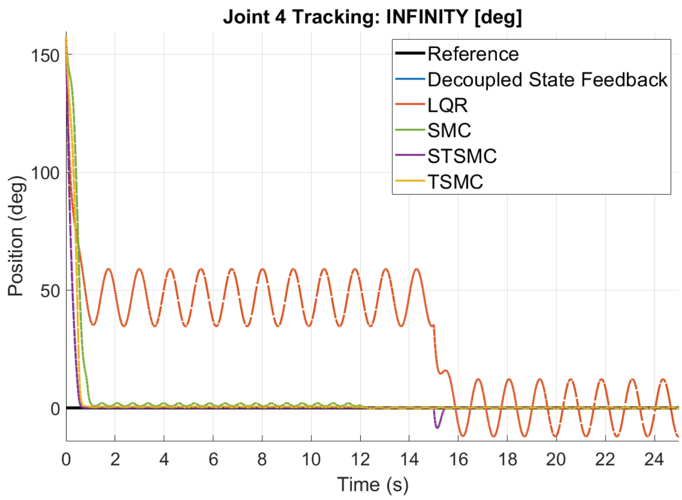

Figure 20: Joint 4 position tracking for the Infinity trajectory.

The position tracking results across the four joints demonstrate that the sliding mode variants successfully maintain the desired figure-eight pattern. The STSMC exhibits the most precise overlay with the reference command, showing negligible visible deviation. Conversely, the Decoupled State Feedback and LQR controllers show significant phase lag and amplitude errors, which would result in a distorted workspace path in a physical application.

To provide a precise comparison of these behaviors, the aggregated performance metrics for this trajectory are summarized in Table 4. These metrics are defined as follows:

- **Root Mean Square Error (RMSE):** Measures the total error energy across the simulation, reflecting overall controller stability.
- **Mean Absolute Error (MAE):** Represents the average tracking deviation, used as the primary metric for path accuracy.
- **Maximum Deviation (D_{max}):** Indicates the peak error recorded during the steady-state phase, serving as a measure of robustness.

Table 4: Global performance metrics for infinity trajectory.

Controller	RMSE (deg)	MAE (deg)	D_{max} (deg)
Decoupled State Feedback	21.6084	9.5643	59.0413
LQR	21.6060	9.5616	59.0412
SMC	9.4420	1.3161	2.1119
STSMC	5.7712	0.4482	8.6462
TSMC	7.9940	0.8599	0.8908

1. **Discussion & Recommendations:**

- **Precision Tracking:** For the infinity path, STSMC is highly recommended for applications where average accuracy is the priority. It achieved an MAE of only 0.4482°, demonstrating that the super-twisting law effectively handles the continuous changes in centrifugal and Coriolis forces without introducing chattering.
- **Robustness to Peaks:** Despite the high average accuracy of other methods, TSMC is the superior choice for maintaining tight control limits, with a D_{max} of 0.8908°. This is nearly ten times lower than the maximum deviation of STSMC 8.6462°, highlighting the advantage of terminal sliding surfaces in constraining peak errors.
- **Performance Comparison:** The data confirms that while STSMC provides the "cleanest" average tracking, TSMC ensures the most reliable performance by preventing large transient spikes. The linear controllers once again failed to provide acceptable results, with an RMSE exceeding 21.6°.

VIII. Conclusion and Future work

This study provided a comprehensive performance evaluation of linear and nonlinear control strategies for a robot arm operating under dynamic disturbances and payload variations. Through the implementation of a modular Simscape architecture, five distinct controllers were tested across three complex trajectories: a parallelogram, a rectangle, and an infinity path.

The simulation results lead to the following key conclusions:

- **High-Precision Tracking:** The STSMC emerged as the superior choice for steady-state accuracy, consistently achieving the lowest MAE (e.g., 0.4449° in the parallelogram path). This confirms the effectiveness of the super-twisting algorithm in eliminating chattering while maintaining tight convergence to the reference.
- **Transient Robustness:** In scenarios involving discontinuous velocity changes or sharp corners, TSMC demonstrated the highest level of robustness. By maintaining a D_{max} significantly lower than all other tested methods (e.g., 0.8297° in the rectangle trajectory), the terminal sliding manifold proved most effective at preventing large error spikes during abrupt transitions.
- **Nonlinear Compensation:** The failure of LQR and Decoupled State Feedback to maintain stability, with RMSE values exceeding 20°, highlights the necessity of nonlinear control for systems experiencing significant gravitational effects and joint coupling.

Future work will focus on the real-time implementation of these strategies on physical hardware to validate the simulation findings and explore adaptive gains for varying payload conditions.

Acknowledgment

This work is financially supported by the French company BIA- TURNKEY TEST SYSTEMS (BiA). The complete fieldwork has been done at the University of Versailles (UVSQ) - Paris Saclay, France.

REFERENCES

[1] M. B. El-Den and A. Hebala, "Challenges in closing the gap between software and hardware in robotics," *Robotics : Integration, Manufacturing and Control*, vol. 1, no. 1, p. 11, Jun. 2024, doi: https://doi.org/10.21622/rimc.2024.01.1.922.

[2] H. Fawzy, A. Elbrawy, M. Amr, O. Eltanekhy, E. Khatab, and O. Shalash, "A systematic review: computer vision algorithms in drone surveillance," *Robotics : Integration, Manufacturing and Control*, vol. 2, no. 1, pp. 1–10, 2025, doi: https://doi.org/10.21622/RIMC.2025.02.1.1149.

[3] Y. Tong, H. Liu, and Z. Zhang, "Advancements in Humanoid Robots: A Comprehensive Review and Future Prospects," *IEEE/CAA Journal of Automatica Sinica*, vol. 11, no. 2, pp. 301–328, Feb. 2024, doi: https://doi.org/10.1109/jas.2023.124140.

[4] S. Sun, H. Huang, and C. Li, "Advancements in humanoid robot dynamics and learning-based locomotion control methods," *Intelligence & Robotics*, vol. 5, no. 3, pp. 631–60, Jul. 2025, doi: https://doi.org/10.20517/ir.2025.32.

[5] A. A. Azhari, W. M. Ahmed, M. F. El-Khatib, and A. Abdellatif, "AI-Driven Trajectory Planning of Dentatron: A Compact 4-DOF Dental Robotic Manipulator," *Biomimetics*, vol. 10, no. 12, p. 803, Dec. 2025, doi: https://doi.org/10.3390/biomimetics10120803.

[6] P. Ferrari *et al.*, "Multi-contact planning and control for humanoid robots: Design and validation of a complete framework," *Robotics and Autonomous Systems*, vol. 166, pp. 104448–104448, May 2023, doi: https://doi.org/10.1016/j.robot.2023.104448.

[7] S. Samadi, J. Roux, A. Tanguy, S. Caron, and A. Kheddar, "Humanoid Control Under Interchangeable Fixed and Sliding Unilateral Contacts," *IEEE Robotics and Automation Letters*, vol. 6, no. 2, pp. 4032–4039, Apr. 2021, doi: https://doi.org/10.1109/lra.2021.3066965.

[8] M. Herrmann, T. Hempel, and A. Al-Hamadi, "A Real-Time Digital Twin Framework for the TIAGo Service Robot," *2025 IEEE International Conference on Systems, Man, and Cybernetics (SMC)*, pp. 6065–6068, Oct. 2025, doi: https://doi.org/10.1109/smc58881.2025.11343553.

[9] J. Wang, Y. Jiang, Y. Li, H. Zhang, and Y. Wang, "A Novel Neural-Network-Based MPC Framework for Whole-Body Motion Optimization and Control of Redundant Humanoid Robots," *IEEE Transactions on Automation Science and Engineering*, vol. 23, pp. 7920–7931, 2026, doi: https://doi.org/10.1109/tase.2026.3679503.

[10] F. Ficuciello, L. Villani, and B. Siciliano, "Variable Impedance Control of Redundant Manipulators for Intuitive Human–Robot Physical Interaction," *IEEE Transactions on Robotics*, vol. 31, no. 4, pp. 850–863, Aug. 2015, doi: https://doi.org/10.1109/tro.2015.2430053.

[11] A. Ajoudani, A. M. Zanchettin, S. Ivaldi, A. Albu-Schäffer, K. Kosuge, and O. Khatib, "Progress and prospects of the human–robot collaboration," *Autonomous Robots*, vol. 42, no. 5, pp. 957–975, Oct. 2017, doi: https://doi.org/10.1007/s10514-017-9677-2.

[12] C. Xu, M. Huang, Z. Liu, and T. Lan, "Collision Detection for Robotic Manipulators using LSTM Autoencoder," *2025 6th International Conference on Control, Robotics and Intelligent System (CCRIS)*, pp. 1–5, Aug. 2025, doi: https://doi.org/10.1109/ccris65764.2025.11192873.

[13] W. Jie, Z. Yudong, B. Yulong, H. H. Kim, and M. C. Lee, "Trajectory Tracking Control Using Fractional-Order Terminal Sliding Mode Control With Sliding Perturbation Observer for a 7-DOF Robot Manipulator," *IEEE/ASME Transactions on Mechatronics*, vol. 25, no. 4, pp. 1886–1893, Aug. 2020, doi: https://doi.org/10.1109/tmech.2020.2992676.

[14] Sushilkumar Ambhore, "A Comprehensive Study on Robot Learning from Demonstration," in *2020 2nd International Conference on Innovative Mechanisms for Industry Applications (ICIMIA)*, Bangalore, India, Mar. 2020, pp. 291–299. doi: https://doi.org/10.1109/icimia48430.2020.9074946.

[15] Z. Xu, X. Yang, and M. Hu, "Nonsingular Terminal Sliding-Mode Control For Robotic Manipulator System With Adaptive Uncertainty and Disturbance Rejection," *2023 China Automation Congress (CAC)*, pp. 7208–7213, Nov. 2023, doi: https://doi.org/10.1109/cac59555.2023.10450478.

[16] S. Ahmed, H. Wang, and Y. Tian, "Adaptive High-Order Terminal Sliding Mode Control Based on Time Delay Estimation for the Robotic Manipulators With Backlash Hysteresis," *IEEE Transactions on Systems, Man, and Cybernetics: Systems*, vol. 51, no. 2, pp. 1128–1137, Feb. 2021, doi: https://doi.org/10.1109/tsmc.2019.2895588.

[17] P. A. Hosseinabadi, A. Soltani, H. Schwartz, H. Pota, and S. Mekhilef, "Fixed-time sliding mode observer-based controller for a class of uncertain nonlinear double integrator systems," *Asian Journal of Control*, vol. 25, no. 5, pp. 3456–3473, Mar. 2023, doi: https://doi.org/10.1002/asjc.3052.

[18] A. Abdellatif, M. E. Asswad, M. Sleiman, K. Khalil, and S. Alfayad, "Composite Hydraulic Integration: A New Step Toward Lightweight Hydraulic Robots," *Malaysian Journal on Composites Science and Manufacturing*, vol. 16, no. 1, pp. 150–166, Apr. 2025, doi: https://doi.org/10.37934/mjcsm.16.1.150166.

[19] E. Amrollah, A. Abdellatif, S. Alfayad, and F. B. Ouezdou, "Performance enhancement of an integrated electro-hydraulic actuator using dynamic modeling and optimization," *Proceedings of the Institution of Mechanical Engineers, Part C: Journal of Mechanical Engineering Science*, vol. 237, no. 12, pp. 2815–2832, Dec. 2022, doi: https://doi.org/10.1177/09544062221142404.

[20] E. A. M., A. A., A. S., and K. K., "Novel Lightweight Hydraulic Integration Methodology for Robotic Applications," *Journal of Advanced Research in Applied Sciences and Engineering Technology*, vol. 49, no. 2, pp. 102–117, Aug. 2024, doi: https://doi.org/10.37934/araset.49.2.102117.